DYNAMICAL DIFFRACTION AS AN ANGULAR SLIT OPTICAL ELEMENT

A Thesis

Presented to the Faculty of the Graduate School

of Cornell University

in Partial Fulfillment of the Requirements for the Degree of

Master of Science

by

Rohit Garg

May 2016

ABSTRACT

X-rays have wavelengths comparable to typical interatomic spacings, which makes them useful for probing the structure of matter on atomic length scales via diffraction. Upcoming developments in x-ray sources and optics promise more coherent flux and smaller beam spots. Focusing a coherent beam to smaller size increases it's angular divergence. This thesis investigates diffraction of coherent, wide angle x-ray beams by ideal crystals using numerical simulations. Detailed calculations of the dynamical diffraction of a Gaussian beam show that diffraction fringes, increased emittance, and movement of the focal plane occur when the angular opening of the beam becomes comparable to the crystal's Darwin width. Simulation of dynamical diffraction of Gauss-Schell beams shows that the diffraction fringes are rapidly smeared out by partial coherence. Further, dynamical diffraction of partially coherent beams may lead to spatial filtering, increasing the reflected beam's coherent fraction and decreasing it's emittance. The novel effects described herein are a consequence of dynamical diffraction being equivalent to a slit in angular space.

BIOGRAPHICAL SKETCH

Rohit Garg was born on December 9, 1985. He received a B. Tech. and M. Tech. (with specialization in nanoscience) in Engineering Physics from Indian Institute of Technology, Bombay in 2010.

This document is dedicated to all Cornell graduate students.

ACKNOWLEDGEMENTS

I have benefited greatly in this work from the assistance and encouragement of my thesis advisors, Joel Brock, Ivan Bazarov, David Sagan and Uli Wiesner. I would also like to thank my fellow students David Agyeman-Budu, Howie Joress and Xin Huang who gave their time, knowledge, and support to make this possible.

TABLE OF CONTENTS

LIST OF TABLES

LIST OF FIGURES

CHAPTER 1

INTRODUCTION

X-ray diffraction has been essential for many fundamental discoveries including the double helix structure of DNA [1] and the structure of quasi-crystals [2]. Improvements in x-ray sources directly affect x-ray experiments and open doors to new experiments. In recent years, the x-ray community has turned it's attention to enhancing the spatial coherence of sources. Examples include SPring-8 II [3] and MAX IV [4] and the broader international effort is reviewed in [5]. Enhanced coherent flux will lead to improvements in techniques like X-ray Photon Correlation Spectroscopy [6], coherent imaging [7], and nanoprobes [8]. There is an ongoing parallel effort to upgrade x-ray optics to utilize these beams [9, 10].

One advantage of increased coherent flux is the ability of focusing beams to smaller spot sizes which is useful for scanning x-ray probes. However, focusing a coherent x-ray beam down to smaller spot sizes necessarily increases the angular divergence. Availability of high coherent flux, wide-angle x-ray beams is a new development in x-ray science. A beam with narrow angular opening can be approximated as a plane wave. The plane wave-matter interaction is well understood both in the kinematic and in the dynamical limit [11]. This thesis studies dynamical diffraction of beams with large angular aperture.

There are two relevant angular scales in the problem, 2α, and θ_D. 2α is the opening angle of the incoming beam. θ_D is the full width at half maximum of the intensity reflectivity. We introduce a unitless parameter,

$$\gamma = 2\alpha/\theta_D \tag{1.1}$$

to measure the disparity between these scales. In the $\gamma \ll 1$ limit, the incoming beam is well approximated by a plane wave. This limit is described by dynamical diffraction theory [11]. When the two angular scales involved become comparable ($\gamma \sim 1$), it is reasonable to expect new phenomena.

We investigate the $\gamma \sim 1$ region of parameter space with numerical simulations. We quantify our results by calculating the intensity pattern, emittance, and focal plane of the outgoing beam. Since no real source is fully coherent, we also explore the region $\gamma \sim 1$ with partially spatially coherent beams.

Our simulations show dynamical diffraction of a Gaussian beam creates fringes (section 5.2), increases emittance (section 5.3) and moves focal plane of outgoing beam by millimeters (section 5.4), when the angular opening of the beam becomes comparable to the crystal's Darwin width. Simulation of dynamical diffraction of partially coherent beams shows that the diffraction fringes are smeared (chapter 8). Diffraction of partially coherent beams can decrease the x-ray beam's emittance (chapter 8).

CHAPTER 2

PARAXIAL OPTICS

2.1 Paraxial Wave Equation

Maxwell's equations in free space reduces to the 3D vector wave equations for the electric field.

$$\nabla^2 \mathbf{E} = \frac{1}{c^2} \frac{\partial^2 \mathbf{E}}{\partial t^2} \tag{2.1}$$

We simplify this equation using 3 assumptions

- The beam is monochromatic
- The beam is linearly polarized everywhere
- The beam is paraxial. That is, the opening angle of the beam cone (which is propagating along the z axis) is small compared to 1 radian

The first two assumptions are encoded in the substitution

$$\mathbf{E} = \hat{\mathbf{u}}\, E(x, y, z)\, e^{ik(z-ct)} \tag{2.2}$$

where $\hat{\mathbf{u}}$ is the polarization direction, E is the slowly varying envelope and $e^{ik(z-ct)}$ is the carrier wave propagating along z axis. The wavelength and speed of the carrier wave are $\lambda = 2\pi/k$ and c respectively. The paraxial approximation is

$$\frac{\partial^2 E}{\partial z^2} \ll k\frac{\partial E}{\partial z} \tag{2.3}$$

Using the substitution in eq 2.2 and the approximation in eq 2.3, eq 2.1 simplifies to,

$$\left(\frac{\partial^2}{\partial x^2} + \frac{\partial^2}{\partial y^2}\right) E(x, y, z) = -2ik\frac{\partial E}{\partial z} \tag{2.4}$$

This equation is the scalar paraxial wave equation [12]. Using the paraxial approximation is suitable for x-ray work because the opening angle of synchrotron radiation is $\sim \gamma_{electron}^{-1} \sim 10^{-4}$ for a 5 Gev electron beam.

Eq 2.4 is similar to the time dependent Schrödinger equation for a free particle where z plays the role of time. Treating eq 2.4 as an initial value problem, fully knowing the electric field at one z value is equivalent to knowing the electric field everywhere. This initial value property simplifies both the formalism, and the numerical code. Any relevant computation can be carried out on E in one plane of constant z. Since all computations for a beam will be done in one constant-z plane, we suppress z from the notation. We describe propagation of paraxial beams in the next section.

2.2 Paraxial Beam Propagation

The Fresnel diffraction integral can be used to propagate the electric field along the z axis. For propagating $E(x, y, z = 0) \rightarrow E(x, y, z_0)$, the Fresnel diffraction integral is given by

$$E(x,y,z=z_0) = \frac{exp(ikz_0)}{2\pi z_0}\ exp\left[\frac{ik(x^2+y^2)}{2z_0}\right]\times \int\int dx'\ dy'\ E(x',y',z'=0)\ exp\left[-\frac{2\pi i(xx'+yy')}{\lambda z_0}\right]\times exp\left[\frac{ik(x'^2+y'^2)}{2z_0}\right] \tag{2.5}$$

2.3 Plane Wave decomposition

Eq 2.4 can be transformed into angular space by a Fourier transform in x and y (eq 2.6). A Fourier Transform is equivalent to decomposing the beam into constituent plane waves. A plane wave of a given u, v propagates at an angle of θ_x from the z axis in the xz plane, and θ_y from the z axis in the yz plane and has the amplitude $\tilde{E}(u,v)$, where $u = \theta_x/\lambda$ and $v = \theta_y/\lambda$.

$$\tilde{E}(u,v) = \int dx\ dy\ E(x,y)e^{2\pi i(xu+yv)} \tag{2.6a}$$

$$E(x,y) = \int du\ dv\ \tilde{E}(u,v)e^{-2\pi i(xu+yv)} \tag{2.6b}$$

$\tilde{E}(u,v)$ can be seen as the angular distribution of plane waves in the beam. Our formalism for plane wave decomposition is adapted from [13]. The primary difference is that we use u (v) instead of θ_x (θ_y) as our angular space variables to simplify numerical implementation.

2.4 Gaussian Beam Description

A Gaussian beam is a solution of the paraxial wave equation in Cartesian coordinates [14]. For a beam propagating along z axis,

$$E(x, y, z = 0) = \exp\left[-\frac{x^2}{w_0^2}\right] \tag{2.7}$$

The waist size, w_0, is the distance from the z axis at which the intensity falls to e^{-2} of it's peak value on the z-axis. The location of the waist is taken to be the $z = 0$ plane. The beam diverges for $z > 0$. The opening half angle of the beam cone is $\alpha = \lambda/\pi w_0$. The Rayleigh range ($z_R = \pi w_0^2/\lambda$) is the distance from the beam waist (measured along z axis) at which the beam area doubles.

A Gaussian beam can also be defined that spans both transverse axes,

$$E(x, y, z = 0) = \exp\left[-\frac{x^2 + y^2}{w_0^2}\right] \tag{2.8}$$

Since eq 2.8 is symmetric in x and y, the results for opening angle, waist size, and Rayleigh range are the same as for Gaussian beam in eq 2.7.

CHAPTER 3

DYNAMICAL DIFFRACTION THEORY

Kinematic scattering (First Born approximation) accurately describes the weak scattering of x-rays by matter. Close to Bragg's condition ($2d\ sin\ \theta = \lambda$), x-ray reflectivity approaches unity and the incoming beam is attenuated inside the crystal. Hence, kinematic scattering is not longer a good description of the physics of diffraction. Dynamical Diffraction theory describes multiple scattering of x-rays by crystalline matter. Original literature on dynamical diffraction by Darwin [15], Ewald [16] and von Laue [17] has been reviewed by Batterman and Cole in [11].

We present our method of solving the equations of dynamical diffraction. We assume that there are two plane waves which are close to satisfying the Bragg's Law.

$$\mathbf{K_H} = \mathbf{K_0} + \mathbf{H} \tag{3.1}$$

E_0 and E_H are the amplitudes of forward and diffracted plane waves respectively. $\mathbf{K_0}, \mathbf{K_H}$ are wavevectors for forward and diffracted wave respectively. The forward and the diffracted plane waves are coupled by the crystal. The crystal is modeled as a medium whose refractive index has the periodicity of the lattice. Upon solving Maxwell's equations in a periodic medium, we obtain

$$\begin{bmatrix} k^2(1-\Gamma F_0) - \mathbf{K_0}.\mathbf{K_0} & -k^2 P\Gamma F_{-\mathbf{H}} \\ -k^2 P\Gamma F_{\mathbf{H}} & k^2(1-\Gamma F_0) - \mathbf{K_H}.\mathbf{K_H} \end{bmatrix} \begin{bmatrix} E_0 \\ E_H \end{bmatrix} = 0 \tag{3.2}$$

Eq 3.2 is the same as eq 16 of [11]. Equation 3.2 is a homogeneous system of linear equations. In eq 3.2,

$$k = |\mathbf{k_0}| \tag{3.3}$$

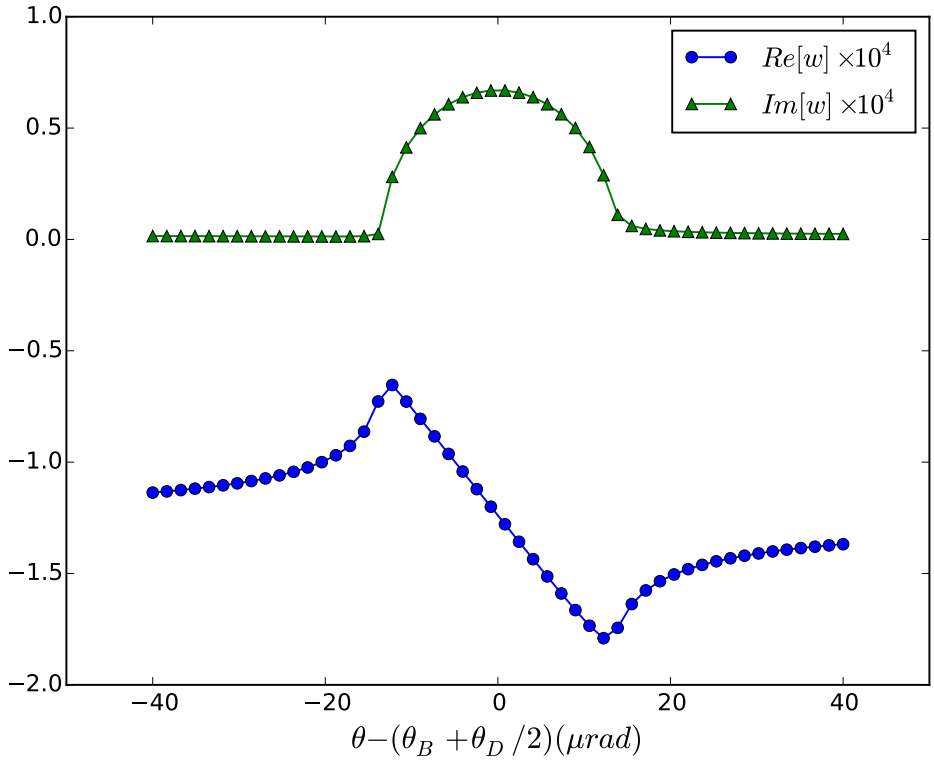

Figure 3.1: (Color Online) w, defined in eq 3.7, near Bragg's condition for Si 111 plane at 10 kev. Blue circles and green triangles denote real and imaginary part respectively. Magnitude of $\mathbf{k_0}$ and w is $\sim O(1)$ and $\sim O(10^{-4})$ respectively.

$\mathbf{k_0}$ and $\mathbf{K_0}$ are wavevectors for the forward wave in-vacuum and in-crystal respectively. The form factors $F_{\mathbf{H}}$ are related to atomic and lattice properties, being defined as

$$F_{\mathbf{H}} = \sum_n (f + f' + if'')_n e^{i\mathbf{H}.\mathbf{r}_n} \tag{3.4}$$

where the summation runs over all the atoms in the basis, and f, f', and f'' are the atomic form factor factor and the dispersion corrections respectively. Γ is a constant defined as

$$\Gamma = \frac{r_e \lambda^2}{\pi V_c} \tag{3.5}$$

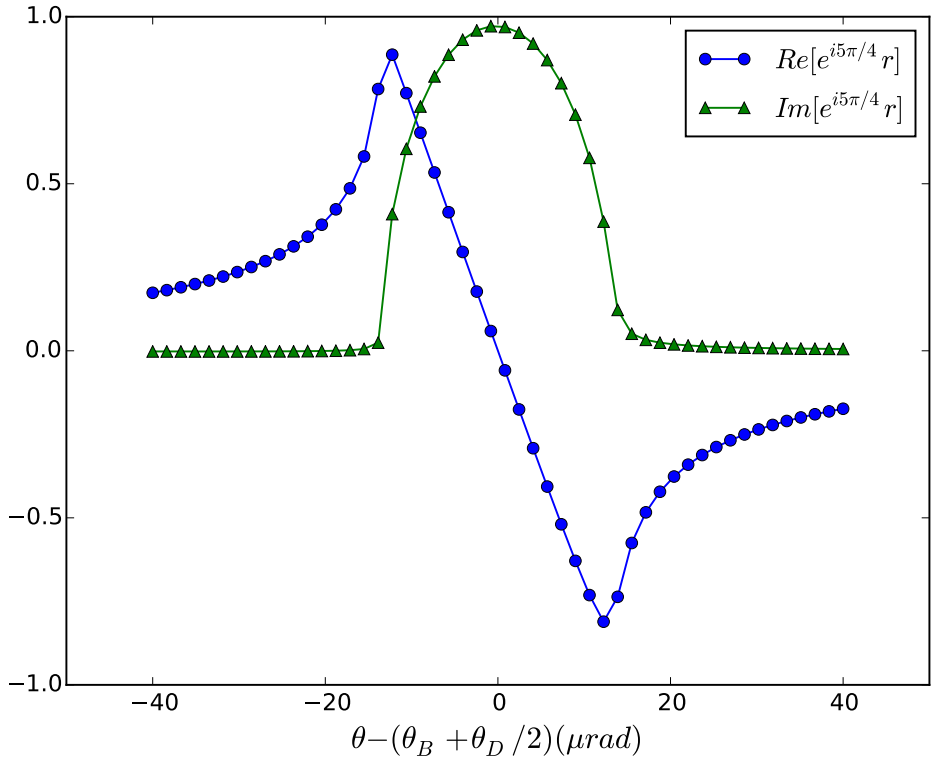

Figure 3.2: (Color Online) Amplitude reflectivity as defined in eq 3.12 for Si 111 plane at 10 kev. Blue circles and green triangles denote real and imaginary part of amplitude reflectivity (r) respectively. The phase factor $e^{i5\pi/4}$ was added to aid visualization of phase of r.

where V_c is the volume of the unit cell and r_e is the classical electron radius. P governs the dependence on polarization by

$$P = \begin{cases} 1 & \text{for } \sigma \text{ polarization,} \\ cos(2\theta) & \text{for } \pi \text{ polarization} \end{cases} \tag{3.6}$$

To satisfy electromagnetic field continuity on the crystal-vacuum interface, we have

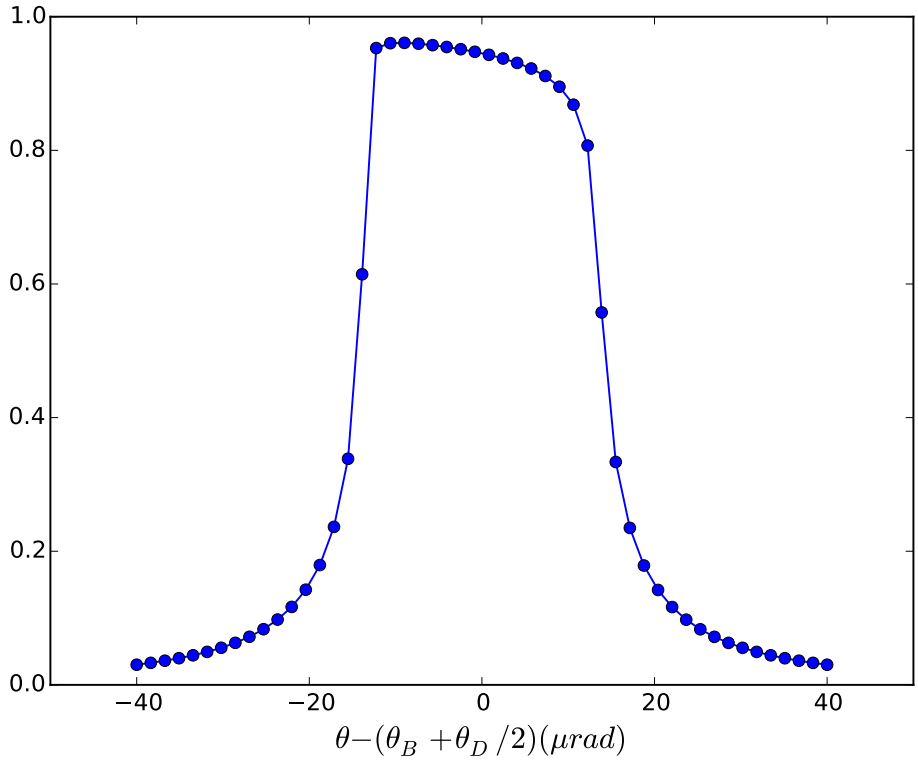

Figure 3.3: (Color Online) Intensity reflectivity as defined in eq 3.12 for Si 111 plane at 10 kev. Reflectivity can be seen as approximately a rectangular aperture in angular domain.

$$\mathbf{K_0} = \mathbf{k_0} + w * \mathbf{n} \tag{3.7}$$

where w is a complex number. Put differently, across an interface, the wavevector can only change along the interface normal. Equation 3.2 can have non-trivial solutions only if

$$\Delta = \det(\mathbf{M}) = 0 \tag{3.8}$$

where

$$\mathbf{M} = \begin{bmatrix} k^2(1-\Gamma F_0) - \mathbf{K_0}.\mathbf{K_0} & -k^2 P\Gamma F_{-\mathbf{H}} \\ -k^2 P\Gamma F_{\mathbf{H}} & k^2(1-\Gamma F_0) - \mathbf{K_H}.\mathbf{K_H} \end{bmatrix} \tag{3.9}$$

Combining eq 3.8 and 3.7, we get

$$\Delta(w) = 0 \tag{3.10}$$

Eq 3.10 combines the relevant variables of incoming wave and the crystal and the boundary conditions. It's a complete description of the dynamical diffraction problem for two plane waves. Eq 3.10 can be solved for various angles of incidence near the Bragg condition ($\mathbf{k_{out}} = \mathbf{k_{in}} + \mathbf{H}$) for a 10 KeV plane wave and Si 111 lattice plane. The solution for w is shown in fig 3.1. We measure length in units of angstroms. Magnitudes of $\mathbf{k_0}$ and w are $\sim O(1)$ and $\sim O(10^{-4})$ respectively.

To obtain the reflectivity (in fig 3.2), we compute non-trivial solutions of

$$\mathbf{M}\begin{bmatrix} E_0 \\ E_H \end{bmatrix} = 0 \tag{3.11}$$

Then, amplitude and intensity reflectivity (r and R) are given by

$$r = E_H/E_0 \tag{3.12a}$$

$$R = rr^* \tag{3.12b}$$

The real and imaginary parts of w in fig 3.1 and the amplitude reflectivity in fig 3.2 behave similarly to the real and imaginary part of the amplitude response function for an underdamped simple harmonic oscillator.

As the incoming plane wave penetrates into the crystal, it is attenuated due to diffraction. The extinction length is defined as the length (measured along **H**) in which the intensity of the incoming beam falls by a factor of e due to diffraction. Figure 3.3 shows the intensity reflectivity due to dynamical diffraction. The full width at half maximum (FWHM) of intensity reflectivity is the Darwin width and is denoted by θ_D.

CHAPTER 4

IMPLEMENTATION DETAILS

4.1 Details of Numerical Experiments

We consider the problem of dynamical diffraction from an ideal semi-infinite crystal. Fig 4.1 shows the geometry of the numerical experiment. The crystal is at the bottom and the vacuum is at the top. The incoming and outgoing beam directions are shown with light blue arrows.

The incoming beam, the beams inside the crystal and the outgoing beam are described in the $(\mathbf{x}_i, \mathbf{z}_i)$, $(\mathbf{x}_c, \mathbf{z}_c)$ and $(\mathbf{x}_o, \mathbf{z}_o)$ frames respectively. To simplify coordinate transformations, the y axes and the origins of these three frames coincide. The three coordinate frames are shown in fig 4.1. An illustration of the incoming and outgoing beams overlaid on $(\mathbf{x}_i, \mathbf{z}_i)$ and $(\mathbf{x}_o, \mathbf{z}_o)$ frames is shown in fig 4.2.

Many variables affect the outgoing beam. To isolate γ dependent phenomena all other variables must be held constant. We used a monochromatic, σ polarized, 10 Kev incoming beam throughout. The crystal was an ideal semi-infinite silicon, and the lattice plane was (111) for all of our calculations. The vacuum-crystal interface was assumed to be ideal. The incident angle was assumed to be at $\theta = \theta_0 = \theta_B + \theta_D/2$. The waist of the incoming beam was always kept at the $z_i = 0$ plane.

As seen in section 2.1, a beam is fully determined by the electric field in a single plane. E_i and E_o denote the electric field of incoming and outgoing beams respectively and are computed in the $z_i = 0$ and $z_o = 0$ planes respectively.

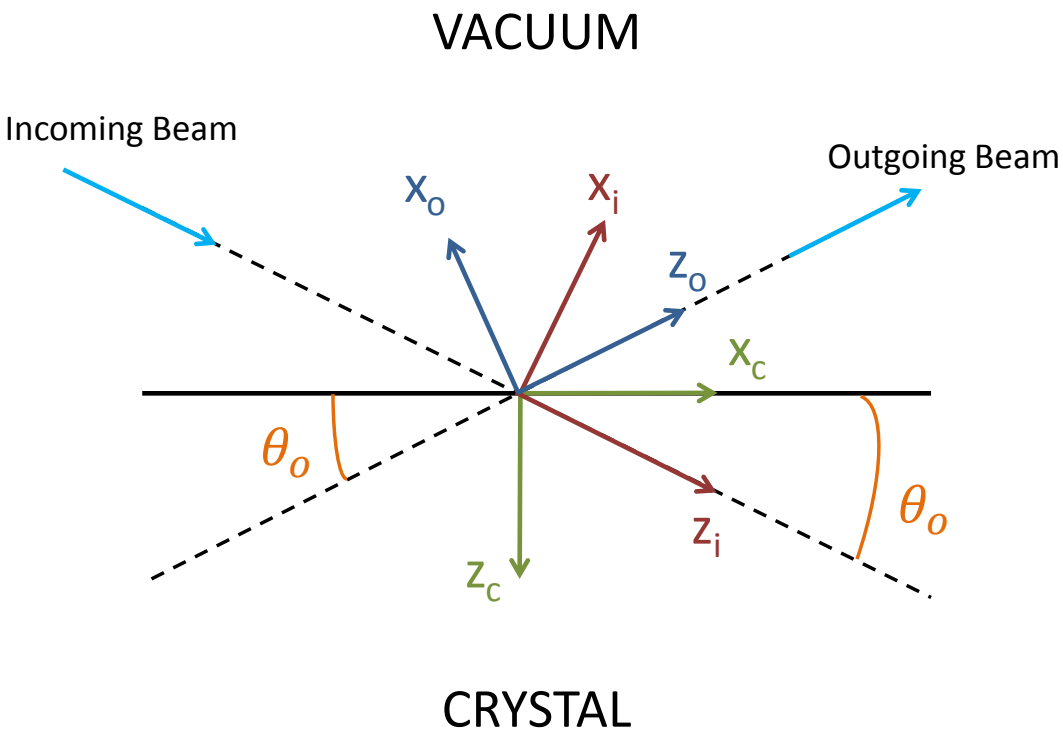

Figure 4.1: (Color Online) Three coordinate frames, local to incoming beam, crystal, and outgoing beam shown in red, green, and blue respectively. The incoming, and outgoing beam's optic axes are along z_i, and z_0 axes respectively. All calculations were done for a σ polarized, monochromatic, 10 Kev beam diffracting off Si 111 plane. Further description in text.

4.2 Algorithm

An algorithm to calculate the dynamical diffraction of x-ray beams must address two needs. First, the equations of dynamical diffraction deal with plane waves, not beams. It is necessary to decompose beams into plane waves, and vice-versa. Second, different coordinate frames are natural for describing the incoming, the outgoing beams, and the dynamical diffraction equations. It is nec-

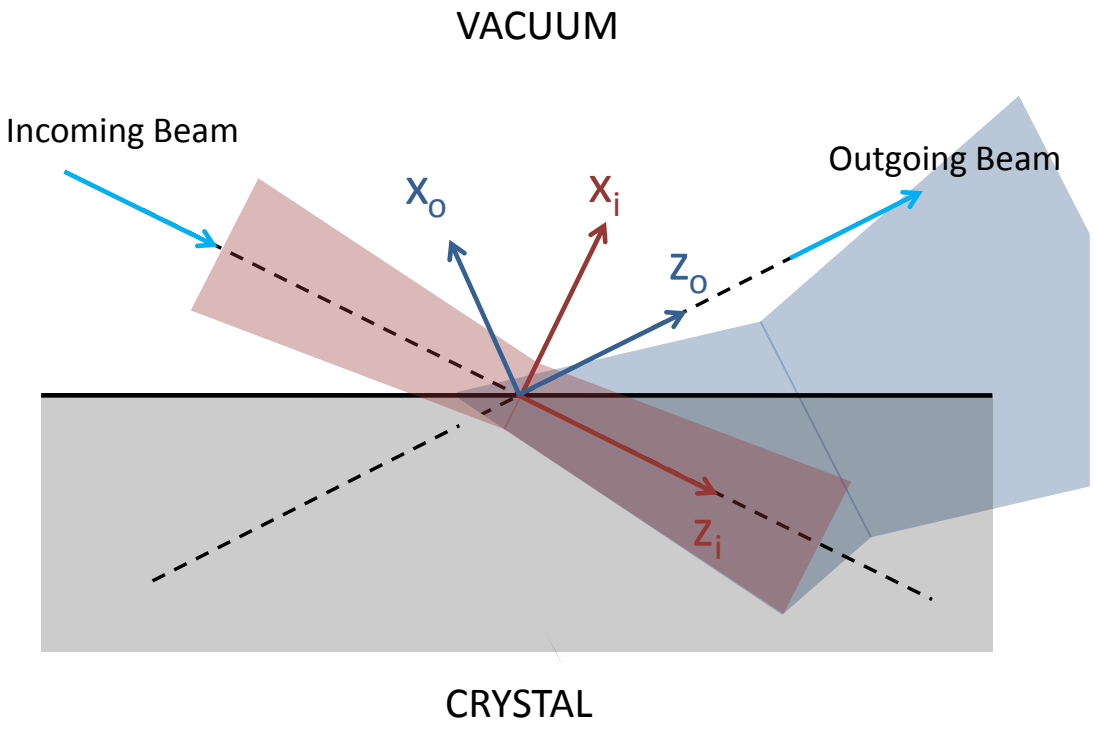

Figure 4.2: (Color Online) An illustration of incoming and outgoing beams relative to the crystal. Red and blue colors are for clarity and do not indicate change in energy of the beam. The outgoing beam also has a waist. The coordinate frames for incoming and outgoing beams are also shown.

essary to perform coordinate transformations between different frames shown in fig 4.1. Coordinate transformation of a plane wave, and beam to plane wave transformations are both straightforward operations. Thus, plane waves serve as a natural bridge between coordinate frames and beams. We adopt the following algorithm to address these needs

1. The incoming beam is decomposed into plane waves in the incoming frame $(\mathbf{x}_i, \mathbf{z}_i)$ by a Fourier Transform

2. The plane waves are coordinate transformed into the crystal frame ($\mathbf{x}_c, \mathbf{z}_c$)
3. An outgoing plane wave is computed for each incoming plane wave by using dynamical diffraction theory.
4. The outgoing plane waves are coordinate transformed into outgoing frame ($\mathbf{x}_o, \mathbf{z}_o$).
5. The outgoing plane waves are summed using an inverse Fourier Transform in the outgoing frame.

4.2.1 Code Details

The code was written in Python 2.7 using the libraries designed for scientific computation including numpy [18], scipy [19] and matplotlib [20]. The performance sensitive portions of the code were implemented in C++ and interfaced to Python using SWIG [21] and ctypes.

Only rotation coordinate transformations were necessary for our simulations. Since we assumed that all plane waves were polarized along y axis, this simplified the plane wave transformations to rotation of just the wavevectors.

A guide for running code developed as part of this thesis is included in appendix B

CHAPTER 5

DYNAMICAL DIFFRACTION OF GAUSSIAN BEAM

5.1 Dynamical Diffraction as an Angular Slit

For a qualitative understanding of dynamical diffraction of a Gaussian beam, it's helpful to think in terms of beam's constituent plane waves. For $\gamma \ll 1$, the wavevectors of almost all of the incoming beam's constituent plane waves lie inside the Darwin Width. These waves are minimally attenuated upon diffraction. The crystal approximately acts like a mirror. For $\gamma \sim 1$, the situation is different. Many of the wavevectors now lie outside the Darwin width. Those outside the Darwin width are not diffracted but are transmitted. Thus, for $\gamma \sim 1$ an ideal crystal acts as a slit in angular space. The results described in this chapter are a consequence of diffraction by an angular slit.

5.2 Fringes in Outgoing Beam

Fig 5.1 shows the intensity pattern for the outgoing beam in the $z_o = 0$ plane when $\gamma = 0.6$. Bragg diffraction produces sinc-like fringes in real space. This is equivalent to Fraunhofer diffraction of a Gaussian beam by a rectangular slit where the slit size is comparable to the beam size.

Experimentally observing these fringes, assuming an ideal monochromatic Gaussian beam were available, would require high spatial resolution. The fringe spacing is $\sim 5\mu m$ in fig 5.1. An area detector must have pixels $\sim 1\mu m$ to resolve the minima of these fringes. A photographic film may have sufficient spatial

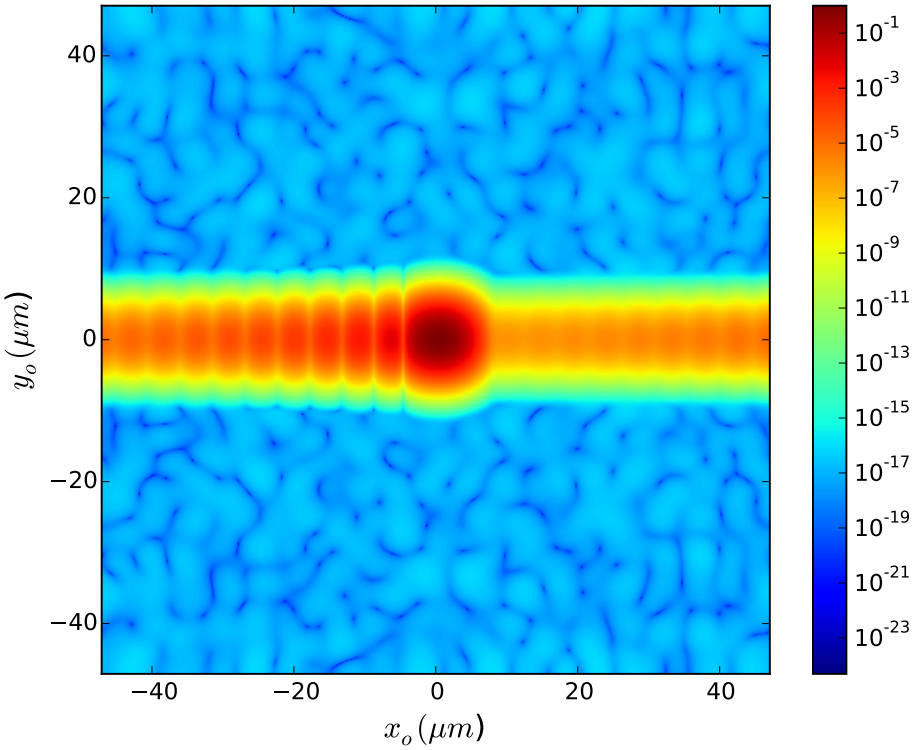

Figure 5.1: (Color Online) Log (base 10) intensity in arb. units of the outgoing beam in $z_o = 0$ plane. $\gamma = 0.6$ for this image. For $\gamma \gtrsim 1$, diffraction acts as a slit in angular space which creates fringes.

resolution.

5.3 Emittance of Outgoing Beam

A Fourier transform maps a signal from the time domain to the frequency domain. The product of the width of the signal in the time domain and the width in the frequency domain has a lower bound. A corresponding property in the space and momentum domain underlies the famous Uncertainty Principle of

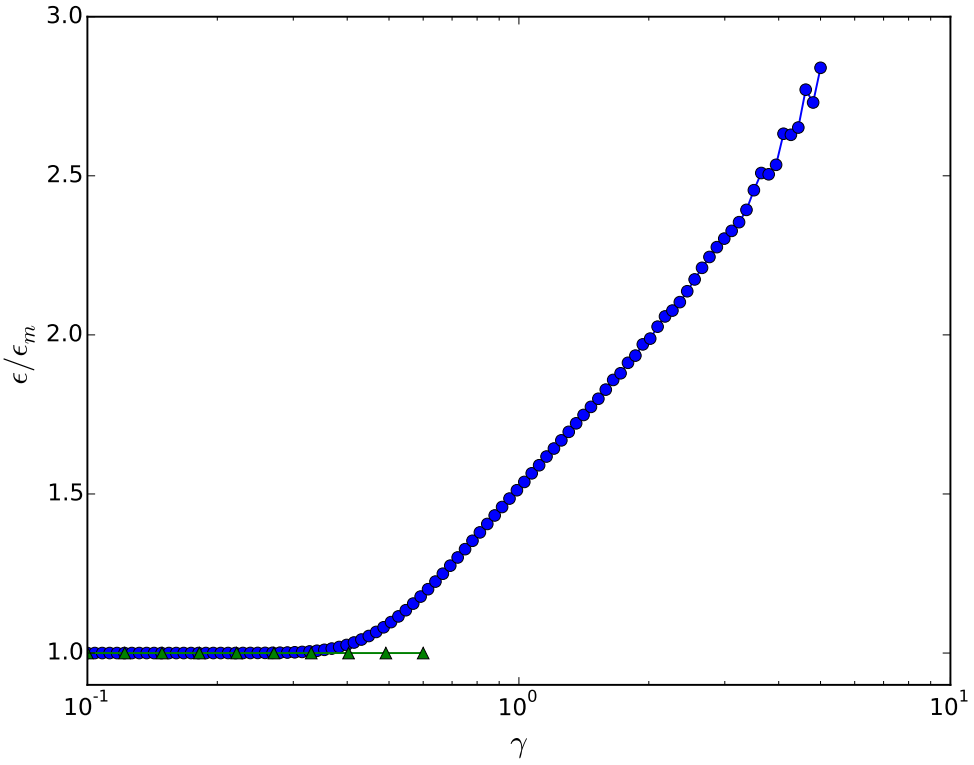

Figure 5.2: (Color Online) Emittance of a Gaussian beam after diffraction. For $\gamma \gtrsim 1$, a Gaussian beam is transformed into a non-Gaussian beam, which has a higher emittance. The emittance along x and y axes is denoted by circles and triangles respectively.

Quantum Mechanics. This is a fundamental property of Fourier transform pairs. For time domain signals, this implies that ultrafast signals must be necessarily broadband signals. x and u are a Fourier pair of variables. The equivalent of the time-bandwidth product for paraxial beams is called emittance.

Lower emittance beams are useful for nanoprobes because they can be focused to a smaller spot. A Gaussian beam has the lowest possible emittance $\epsilon = \epsilon_m = \lambda/4\pi$. All other beams, coherent or incoherent, have a higher emittance. The emittance is not a measure of spatial coherence [22]. For example, Hermite-

Gaussian modes (further described in chapter 6) have higher than minimum emittance, but are fully coherent. A beam with minimum emittance is also described as a diffraction limited beam.

5.3.1 Emittance Formalism

We adapt our emittance formalism from [13]. Emittance along x axis is defined as

$$\frac{\epsilon^2}{\epsilon_m^2} = 1 + 16\pi^2 \left[\langle x^2 \rangle \langle u^2 \rangle - \langle xu \rangle \langle ux \rangle \right] \tag{5.1}$$

where $\epsilon_m = \lambda/4\pi$, the minimum emittance. The statistical moments in eq 5.1 are

$$\langle x^2 \rangle = \int \int dxdy \; E(x,y)^* x^2 E(x,y) \tag{5.2a}$$

$$\langle u^2 \rangle = \frac{1}{4\pi^2} \int \int dxdy \; \frac{\partial E(x,y)}{\partial x} \frac{\partial E(x,y)^*}{\partial x} \tag{5.2b}$$

$$\langle xu \rangle = \frac{1}{2\pi i} \int \int dxdy \; E(x,y)^* x \frac{\partial E(x,y)}{\partial x} \tag{5.2c}$$

$$\langle ux \rangle = \frac{-1}{2\pi i} \int \int dxdy \; E(x,y) x \frac{\partial E(x,y)^*}{\partial x} \tag{5.2d}$$

Note that $\langle ux \rangle$ and $\langle xu \rangle$ in eq 5.2 are complex conjugates. Extending this formalism to the y axis is straightforward.

5.3.2 Results

A Gaussian beam, with $\gamma \sim 1$, is no longer Gaussian after diffraction from an ideal crystal (fig 5.1). All non-Gaussian beams have a higher than minimum emittance. The variation of the emittance in the $z_o = 0$ plane with γ is shown in fig 5.2. γ was changed by changing the opening angle (α) of the incoming beam. Here wavelength, crystal and θ_D was kept constant.

Emittance results in fig 5.2 for x and y axes are from different simulations due to resource constraints. The emittance along the x axis was calculated using a 1D beam from eq 2.7. The 1D Gaussian beam was discretized into 2^{19} plane waves. The emittance along the y axis was calculated for a 2D beam using eq 2.8. This 2D Gaussian beam was discretized into 4096 x 4096 plane waves. $\gamma = 0.6$ is the upper limit for 2D Gaussian beam simulations due to resource constraints. The results for the y axis show no effect on the out of plane component of the emittance. The effects of dynamical diffraction are limited to the xz plane as shown in fig 4.1.

Fig 5.2 shows that a diffraction limited beam diffracting off an ideal crystal can become non-diffraction limited. The increase in emittance near $\gamma = 1$ means that a monochromator should be evaluated for emittance preservation if delivering a diffraction limited beam to the sample is a goal.

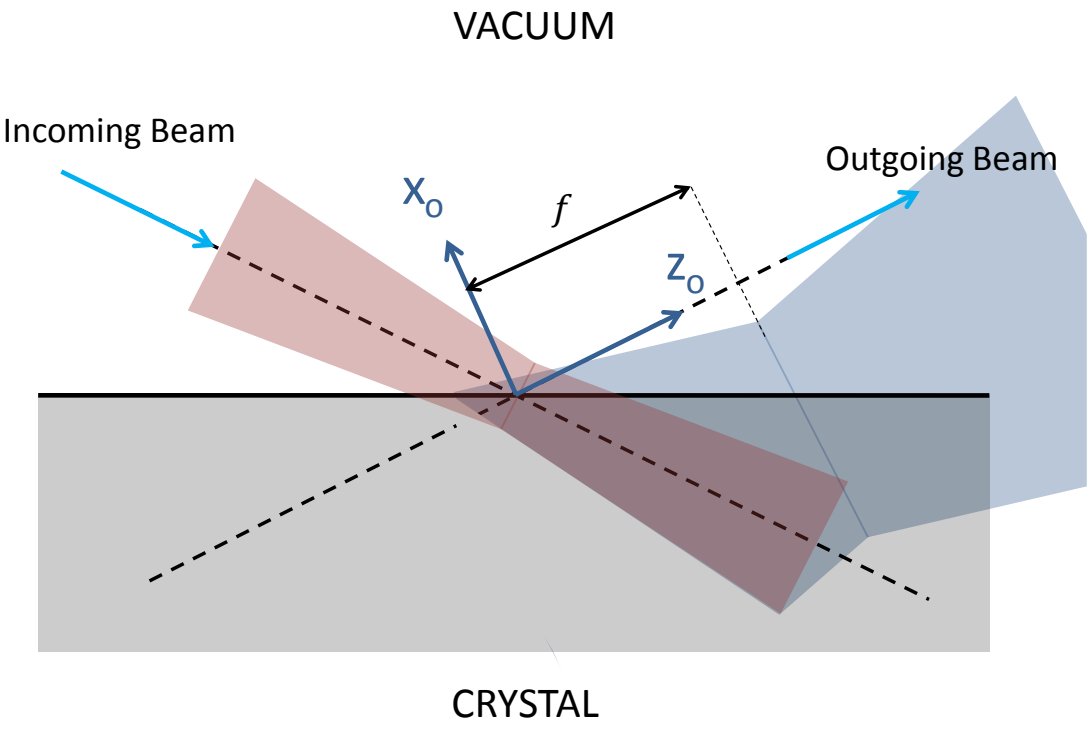

Figure 5.3: (Color Online) The outgoing beam also has a waist in the $(\mathbf{x}_o, \mathbf{z}_o)$ plane. The distance of the focal plane from $z_o = 0$ plane is denoted by f. Note that outgoing beam may have a virtual focus.

5.4 Focus Position of Outgoing Beam

Beams have well defined focal planes. From the electric field in one plane perpendicular to optic axis, the focal plane of the beam along either axis can be calculated. This distance to focal plane on the x axis (adapted from [13]) is

$$z_s = -\frac{\langle xu \rangle + \langle ux \rangle}{2\lambda \langle u^2 \rangle} \tag{5.3}$$

The focal plane for y axis is calculated by a similar formula. We calculate the position of the virtual focus for the outgoing beam along z_o axis, relative to the

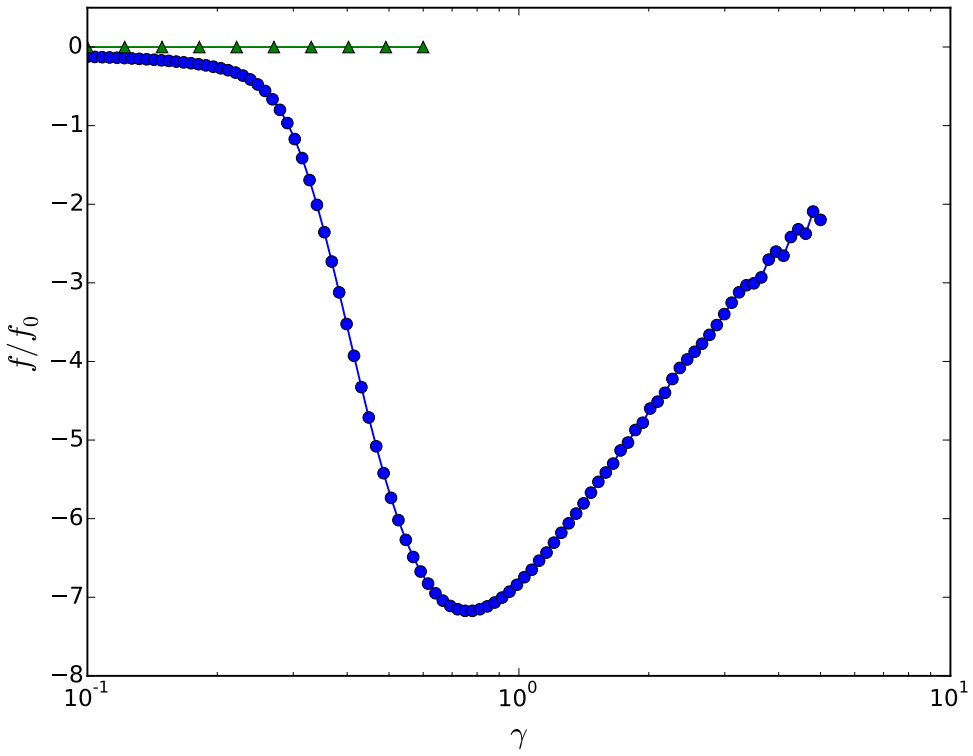

Figure 5.4: (Color Online) Position of outgoing beam's focus, measured along z_o axis, relative to $z_o = 0$. Focal plane position along x and y axes is denoted by circles and triangles respectively.

$z_o = 0$ plane. A schematic illustration is shown in fig 5.3. We adopt $f_0 = \pi l_e^2/d$ as the measuring unit for focus position. Here, l_e and d are extinction length and lattice plane spacing respectively. f_0 is independent of γ. For Si 111 at 10 kev, $f_0 = 1.6\ mm$.

The focus position for outgoing beams is shown in fig 5.4. Focal plane olcation results in fig 5.4 for x and y axes are from different simulations due to resource constraints. The focal plane along the x axis was calculated using a 1D beam from eq 2.7. The 1D Gaussian beam was discretized into 2^{19} plane waves. The focal plane along the y axis was calculated for a 2D beam using eq 2.8.

This 2D Gaussian beam was discretized into 4096 x 4096 plane waves. As with emittance results (section 5.3), the results for y axis show no effect on the out of plane component. Since the focal planes for x and y do not coincide along z axis (except near $\gamma \ll 1$), the outgoing beam is astigmatic.

We note a minimum at $\gamma = 0.78$. We emphasize that $\gamma \sim 1$ should be seen as a region of parameter space where new phenomena are seen because two relevant angular scales are comparable. However, the point $\gamma = 1$ is not necessarily special since our definition of angular scale, and hence γ, is well defined only to within small numerical factors.

5.5 Focus movement Conjecture

To investigate the cause of the minimum in fig 5.4, we calculate the location of the focal plane of a 1D Gaussian beam after diffraction by a slit in real space. A schematic drawing is shown in fig 5.5. This is the real space equivalent of dynamical diffraction by a crystal. The scale parameter here (the analog of γ) is $\beta = w_0/a$. The waist of a Gaussian beam is w_0 and the slit size is $2a$. The incoming beam's waist is located in the plane of the slit. The position of the outgoing beam's focus is measured relative to the slit plane. We keep w_0 fixed and let a vary with β. Since w_0 is fixed, we can use the Rayleigh range ($z_R = \pi w_0^2/\lambda$) of the incoming beam as a measuring unit for the location of the focal plane. The results are shown in fig 5.6.

The similarity of shape between fig 5.6 and 5.4 suggests that the movement of focus in fig 5.4 is a property of slit diffraction of a Gaussian beam.

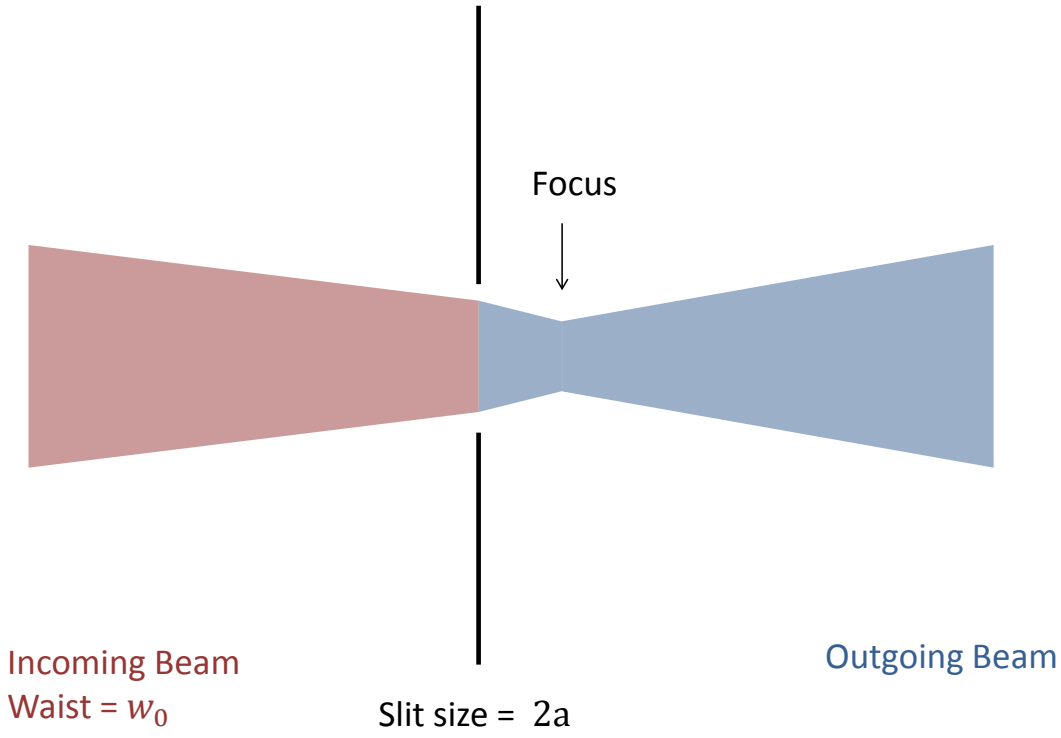

Figure 5.5: (Color Online) Schematic diagram of a monochromatic Gaussian beam diffracting off a slit in real space. The incoming and outgoing beams are shown in red and blue respectively for clarity. This does not indicate change in energy of the beam. The focus of the incoming beam is at the plane of the slit. The focal plane of the outgoing beam is not at the plane of the slit due to diffraction.

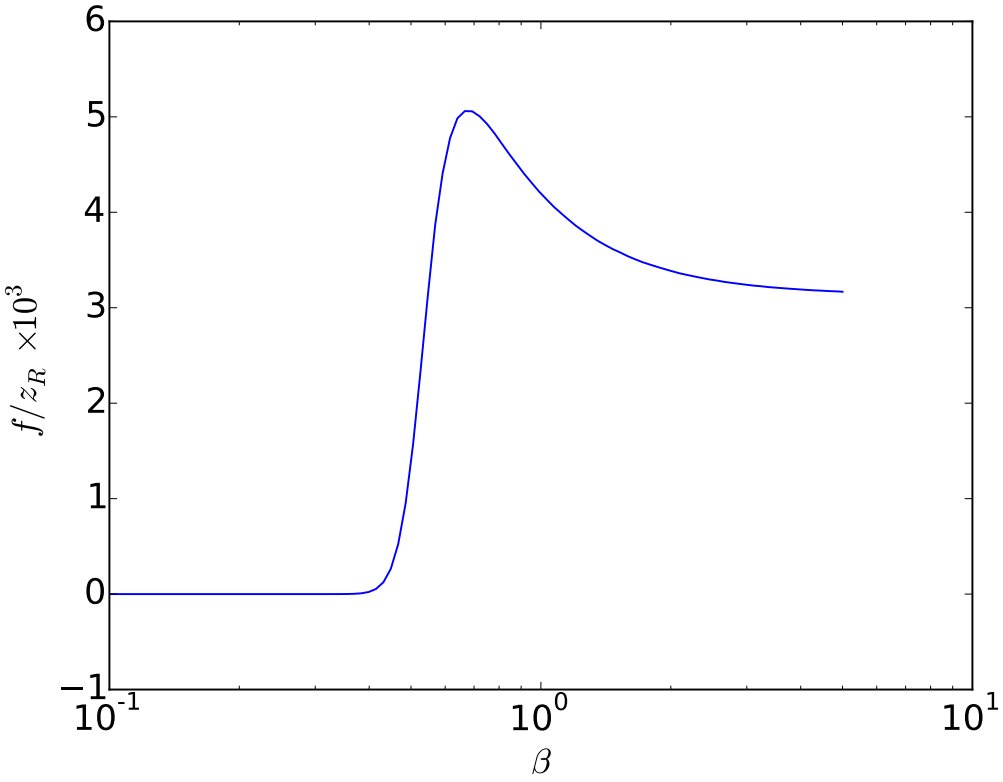

Figure 5.6: (Color Online) Position of a Gaussian beam's focus after diffraction from a slit in real space. Focus position is measured relative the plane of slit. This plot is similar to fig 5.4.

CHAPTER 6

DYNAMICAL DIFFRACTION OF HERMITE GAUSSIAN MODES

Hermite-Gaussian (HG) modes are a family of higher order solutions [14] of the paraxial wave equation (see eq 2.4). In 1D, they are

$$E_m(x, z = 0) = H_m\left(\frac{\sqrt{2}x}{w_0}\right)\exp\left[-\frac{x^2}{w_0^2}\right] \tag{6.1}$$

Here $H_m(x)$ are the Hermite polynomials. The lowest order (m=0) HG mode is the Gaussian mode (eq 2.7) itself. Angular rms size (α_m), real space rms size (w_m), and emittance (ϵ_m) of m^{th} order HG mode are related to it's Gaussian counterpart (m=0) by

$$\alpha_m = \sqrt{2m+1}\alpha_0 \tag{6.2a}$$

$$w_m = \sqrt{2m+1}w_0 \tag{6.2b}$$

$$\epsilon_m = (2m+1)\epsilon_0 \tag{6.2c}$$

respectively. HG modes can be generalized to two dimensions.

$$E_{mn}(x, y, z = 0) = E_m(x, z = 0)E_n(y, z = 0) \tag{6.3}$$

HG modes of eq 6.3 are a family of orthogonal functions which form a complete basis set. Any solution of the paraxial wave equation can be written as a linear superposition of HG modes. Since the HG modes in two dimensions can be factorized into a product of functions along x and y, eq 6.2 holds for 2D HG modes as well.

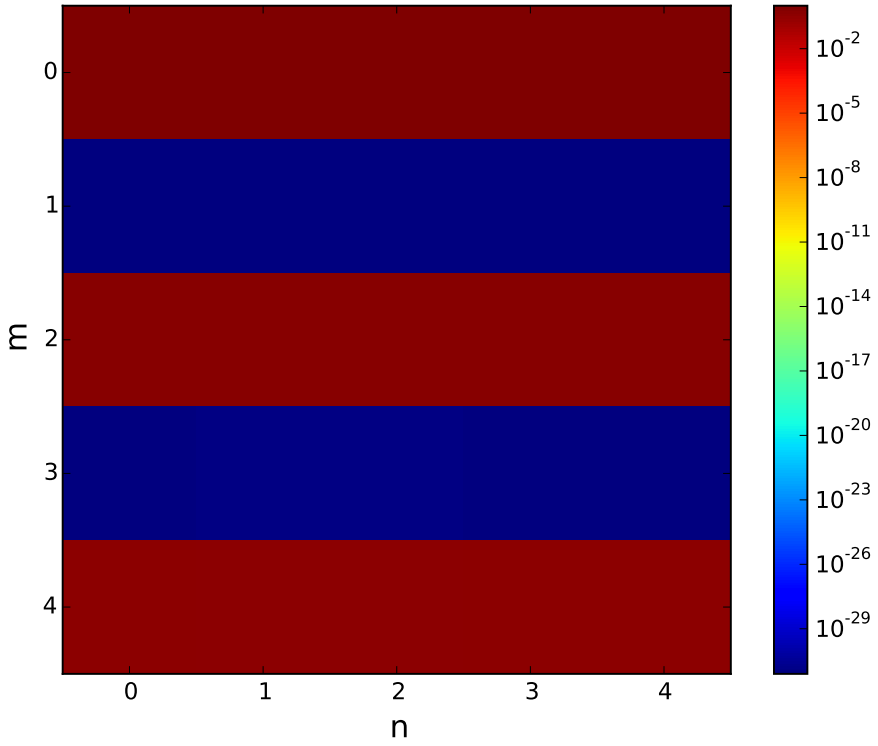

Figure 6.1: (Color Online) I_{rx}^{mn} values (defined in eq 6.5) in arb. units for γ = 0.6. Almost zero ($\sim 10^{-30}$) intensity for odd modes in x (indexed by m) suggests odd/even symmetry is pseudo-preserved after dynamical diffraction.

Hermite polynomials have odd/even symmetry. It follows that HG modes have odd/even symmetry if the mode index m/n is odd or even. We ask if odd/even symmetry is preserved after dynamical diffraction of a HG mode. Fig 5.1 shows the intensity pattern for the Gaussian mode. This pattern is neither even nor odd. Thus, in general dynamical diffraction does not preserve the odd/even symmetry of the incoming beam.

There also exists a weaker form of odd symmetry. That is

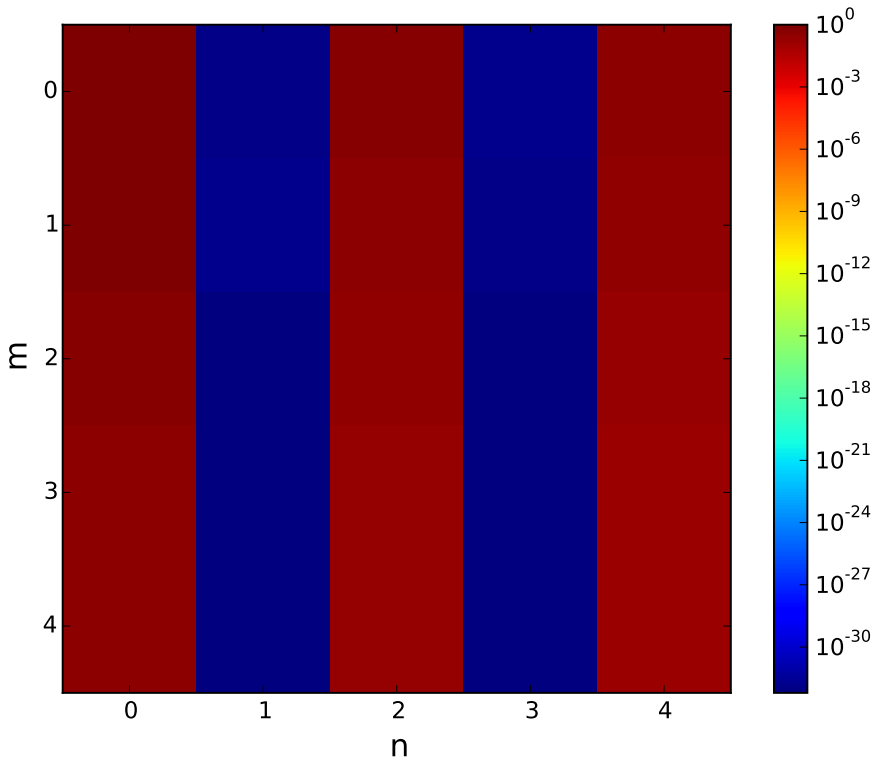

Figure 6.2: (Color Online) I_{ry}^{mn} values (defined in eq 6.5) in arb. units for γ = 0.6. Almost zero ($\sim 10^{-30}$) intensity for odd modes in y (indexed by n) suggests odd/even symmetry is pseudo-preserved after dynamical diffraction.

$$\int_{-\infty}^{\infty} dx\ f(x) = 0 \tag{6.4}$$

We ask if dynamical diffraction preserves the weak form of odd symmetry. This question can be answered by computing what we call amplitude-then-intensity integration. The electric field for the incoming beam, which is in (m,n) HG mode, is denoted by E_i^{mn}. Denote electric field for outgoing beam by E_o^{mn}. Define,

$$I_{rx}^{mn} = \int dy_o \left| \int E_o^{mn} dx_o \right|^2 \tag{6.5a}$$

$$I_{ry}^{mn} = \int dx_o \left| \int E_o^{mn} dy_o \right|^2 \tag{6.5b}$$

I_{rx}^{mn} (I_{ry}^{mn}) is an integral of a purely positive quantity $\left|\int E_o^{mn} dx_o\right|^2$ ($\left|\int E_o^{mn} dy_o\right|^2$). Thus,

$$I_{rx}^{mn} = 0 \Rightarrow \int E_o^{mn} dx_o = 0 \tag{6.6}$$

I_{rx}^{mn} and I_{ry}^{mn} can be written in matrix form. These two matrices are shown in visual form in figures 6.1 and 6.2 respectively. In fig 6.1 (6.2), we see that I_{rx}^{mn} (I_{ry}^{mn}) is approximately zero ($\sim 10^{-30}$) whenever m (n) is odd. Exact values of I_{rx}^{mn} and I_{ry}^{mn} matrices are shown in appendix A. We conclude that dynamical diffraction preserves the weak form of odd symmetry of HG modes.

CHAPTER 7

PARTIAL SPATIAL COHERENCE

7.1 Partially coherent beams

Any solution of the paraxial wave equation can be written as a superposition of Hermite-Gaussian modes (eq 6.3). The superposition coefficients may be complex-valued. Decoherence is equivalent to loss of knowledge of the relative phase of the constituent Hermite-Gaussian modes. The electric field of a partially coherent beam is ill-defined without knowing the relative phase of coefficients. Instead, the cross-spectral density (Γ) is used to specify partially coherent beams. For quasi-monochromatic beams, cross spectral density [23] is

$$\Gamma(\mathbf{r}_1, \mathbf{r}_2, \omega) = \int \langle E(\mathbf{r}_1, t) E^*(\mathbf{r}_2, t+\tau) \rangle_t \, e^{i\omega\tau} d\tau \tag{7.1}$$

The subscript (t) means ensemble average over time. Since we are dealing with a monochromatic component, we suppress ω from the notation going forward. The transition from electric field to cross-spectral density is analogous to the transition from wave function ($|\psi\rangle$) to density matrix ($\hat{\rho}$) in Quantum Mechanics [24].

7.2 Gauss-Schell Model

Modern undulator based x-ray sources produce radiation from electron bunches containing a large number of particles ($\sim 10^{10}$). All electrons radiate indepen-

dently and there is no phase relationship between radiation from different electrons. The resulting beam is partially coherent both spatially and temporally.

Calculating the full synchrotron radiation from an electron bunch with $\sim 10^{10}$ particles is an involved computation. We make progress by modeling the synchrotron radiation using a Gauss-Schell model. The Gauss-Schell model (GSM) has been empirically observed to be a good approximation of the monochromatic component of synchrotron radiation [25, 26, 27]. GSM defines the monochromatic component of a one-dimensional source by a cross-spectral density [28] of the form

$$\Gamma(x_1, x_2) = \Gamma_0 \exp\left[-\frac{x_1^2 + x_2^2}{2\sigma_I^2}\right] \exp\left[-\frac{(x_1 - x_2)^2}{2\sigma_\mu^2}\right] \tag{7.2}$$

where $\Gamma_0, \sigma_I, \sigma_\mu$ are positive constants. The GSM can also be expressed as a superposition of incoherent HG modes

$$\Gamma(x_1, x_2) = \sum_{n=0}^{\infty} \lambda_n \phi_n(x_1) \phi_n^*(x_2) \tag{7.3}$$

where $\lambda_n = \lambda_0 q^n$, $\phi_n(x) = c_n H_n\left(\sqrt{2}x/w\right) e^{-x^2/w^2}$, and c_n is a normalization constant chosen to make $\int \phi_n^2 dx = 1$. q is a unitless number ($0 \leq q < 1$) which changes the relative energy of the modes. The beam is fully coherent and fully incoherent in the $q \to 0$ and $q \to 1$ limits respectively. Hence, the coherence of the beam varies with q.

7.3 Implementation details

For numerical work, the expansion in eq 7.3 is truncated to N terms. The truncated terms have a fraction $\epsilon_{GSM} = q^N$ of the total energy. We choose $\epsilon_{GSM} = 10^{-2}$, and let N vary, which changes the coherence of the beam. For example, a beam where 2 modes have 99% of the energy is more coherent than one where 3 modes have 99% of the energy.

We define coherent fraction f_c as the fraction of the total energy (in the untruncated beam) in the n=0 mode. The coherent fraction is related to N by $f_c = 1 - \sqrt[N]{\epsilon_{GSM}}$. There is one exception to this formula for f_c. A beam where the n=0 mode has 99% of the total energy is partially coherent in theory. But since only one mode is simulated, in practice, the simulation for N=1 is equivalent to fully coherent beam.

Going from coherent modes to incoherent beams requires repeating the algorithm described in section 4.2 once for each incoherent mode. To calculate intensity of the outgoing beam, the intensity of all constituent incoherent modes can be added directly. However, the emittance and focus formulas in eq 5.1, and 5.3 are based on the electric field, and are unsuitable for partially coherent beams. Emittance and focus formulas for incoherent beams are described in the next section.

7.4 Wigner Distribution Function

The electric field is not well defined for partially coherent beams. Hence, the emittance and focal distance formulas given in section 5.3, and 5.4 cannot be

used for partially coherent beams. The Wigner Distribution Function (WDF) has been discussed in the literature for studying partially coherent synchrotron radiation [29, 22]. We use the WDF for calculating the emittance and the focal plane of partially coherent beams. Our formalism for the WDF is adapted from [30]. The primary difference is that we rescale u in [30] to match our definition $u = \theta/\lambda$.

For a coherent mode, the WDF is defined as

$$W(x,u) = \int dx\ E(x - x'/2)E^*(x + x'/2)e^{2\pi i x' u} \tag{7.4}$$

x, and u in eq 7.4 are the same as in eq 2.6. For an incoherent superposition of two modes, the Wigner Distributions of the two modes add directly

$$W = W_1 + W_2 \tag{7.5}$$

The WDF for the outgoing beam is calculated by calculating the WDF for each mode using eq 7.4, and then adding up the WDFs using eq 7.5. Defining $W_0 = \int dx\ du\ W$, the WDF can be considered a quasi-probability distribution in (x, u) phase space after normalizing by W_0. The WDF is not a true probability distribution because the WDF can take negative values. However, WDF is always real-valued. This quasi-probability distribution can be used to define statistical moments of the beam.

$$\langle x \rangle_W = \frac{1}{W_0} \int dx\ du\ x\ W \tag{7.6a}$$

$$\langle u \rangle_W = \frac{1}{W_0} \int dx\, du\, u\, W \tag{7.6b}$$

$$\langle x^2 \rangle = \frac{1}{W_0} \int dx\, du\, (x - \langle x \rangle_W)^2\, W \tag{7.6c}$$

$$\langle u^2 \rangle = \frac{1}{W_0} \int dx\, du\, (u - \langle u \rangle_W)^2\, W \tag{7.6d}$$

$$\langle xu \rangle_W = \frac{1}{W_0} \int dx\, du\, (x - \langle x \rangle_W)(u - \langle u \rangle_W)\, W \tag{7.6e}$$

Emittance is defined in terms of the statistical moments defined in eq 7.6,

$$\frac{\epsilon}{\epsilon_m} = 4\pi \sqrt{\langle x^2 \rangle \langle u^2 \rangle - \langle xu \rangle_W^2} \tag{7.7}$$

The factor of 4π is necessary to match the results from eq 5.1. Similarly, the distance to the focal plane is given by

$$z_s = -\frac{\langle xu \rangle_W}{\lambda \langle u^2 \rangle} \tag{7.8}$$

CHAPTER 8

DYNAMICAL DIFFRACTION OF PARTIALLY COHERENT BEAMS

In eq 7.3, q and w determine the coherence and spot size of a GSM beam respectively. Combining the definition of γ and α, we get

$$\gamma = \frac{2\ \lambda}{\theta_D\ \pi\ w} \tag{8.1}$$

Thus, choosing γ is equivalent to choosing w in eq 7.3. All modes in eq 7.3 have the same w. We set $\epsilon_{GSM} = 10^{-2}$ and calculate q using $\epsilon_{GSM} = q^N$ where N is the number of constituent modes. This fully specifies all constituent modes of a GSM beam. Due to resource constraints, the upper limit for GSM beams in our simulations is $\gamma = 0.6$.

Both spatial and temporal incoherence contribute to smearing of fringes in fig 5.1. We observe spatial incoherence induced smearing in fig 8.1. The simulation shown in fig 8.1 was carried out using a 1D Gaussian beam, discretized into 8192 plane waves. We notice that the fringes are very sensitive to partial coherence of the beam. For a coherent fraction of 79%, the fringe visibility is close to minimal.

The calculation in fig 8.1 is for purely monochromatic beam. Temporal incoherence also contributes to fringe smearing. Our calculations show that an incoming Gaussian beam with an energy bandwidth $\Delta E/E = 10^{-4}$ produces no measurable fringe smearing. This suggests that with further development, this effect might prove to be a useful proxy for measuring spatial, and temporal coherence.

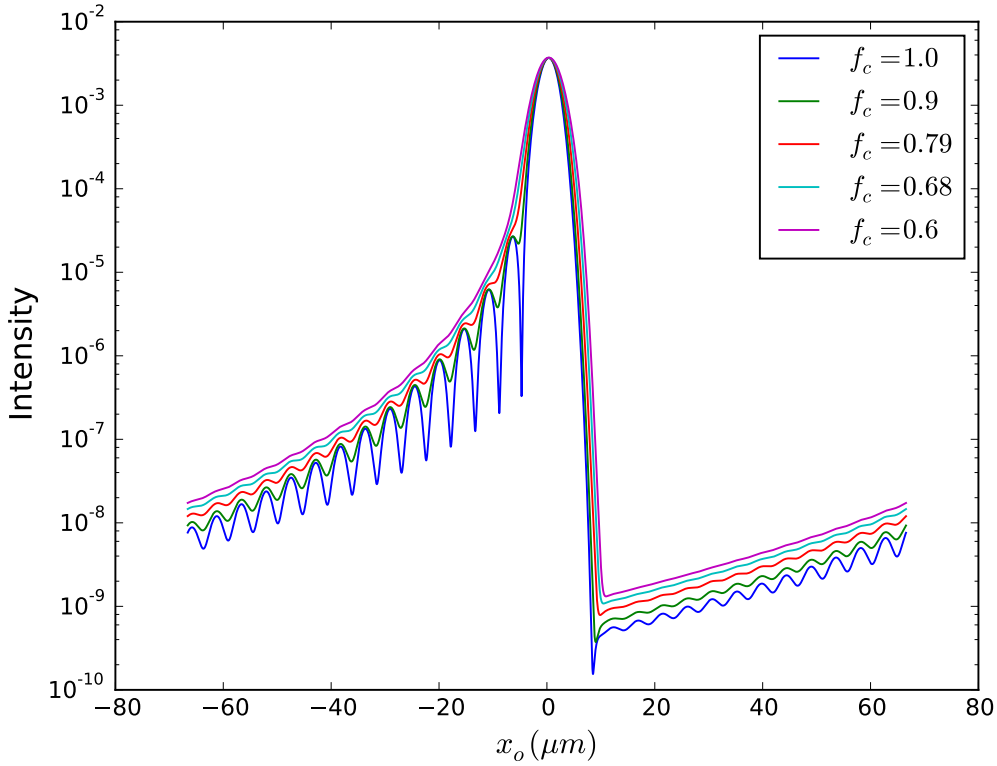

Figure 8.1: (Color Online) Intensity along x_o axis at $z_o = 0$ plane for the Gauss-Schell Model incoming beam ($\gamma = 0.6$) in arb. units. Legend denotes the coherent fraction of incoming beam. The fringes created by an angular slit are smeared out due to spatial incoherence.

We calculated emittance of outgoing beam using eq 7.7. Our results for the emittance of an outgoing beam is shown in fig 8.2. The simulation shown in fig 8.2 and 8.3 was carried out using a 1D Gaussian beam, discretized into 8192 plane waves. For $\gamma \ll 1$, the emittance does not change with γ for both fully, and partially fully coherent beams. But near $\gamma = 0.6$, the emittance declines for more incoherent beams.

Higher order HG modes have a larger angular size than lower order modes (eq 6.2). If near $\gamma = 0.6$, the higher order modes are being attenuated more

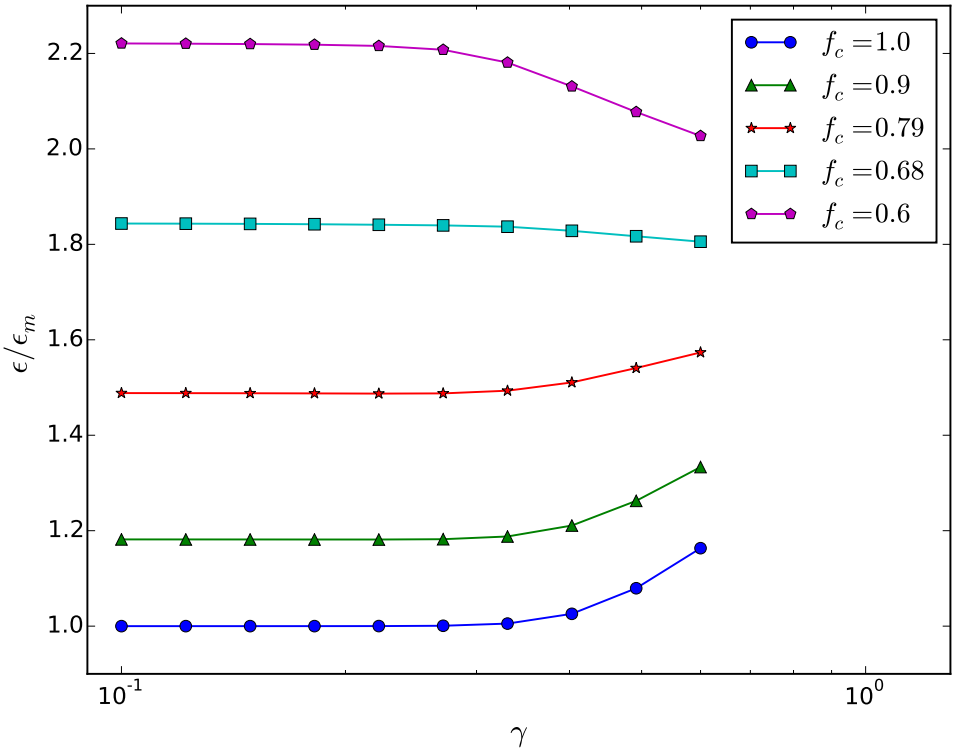

Figure 8.2: (Color Online) Emittance of the outgoing beam as a function of the incoming beam's coherence and γ. The emittance calculated in z_0 = 0 plane. Legend denotes the coherent fraction of the incoming beam. Horizontal axis is graduated on a logarithmic scale.

by the angular slit, this would increase the weight of the lower order modes in the outgoing beam. This increases coherent fraction of the outgoing beam, lowering it's emittance. We speculate that this is the cause behind the reduction in emittance near γ = 0.6 for more incoherent beams in fig 8.2

We calculated the distance to the focal plane for the outgoing beam using eq 7.8. Our results for focus position of the outgoing beam are presented in fig 8.3. Our simulations show that unlike the fringes which smear out due to incoherence (fig 8.1), the movement of the focal plane is robust with respect to

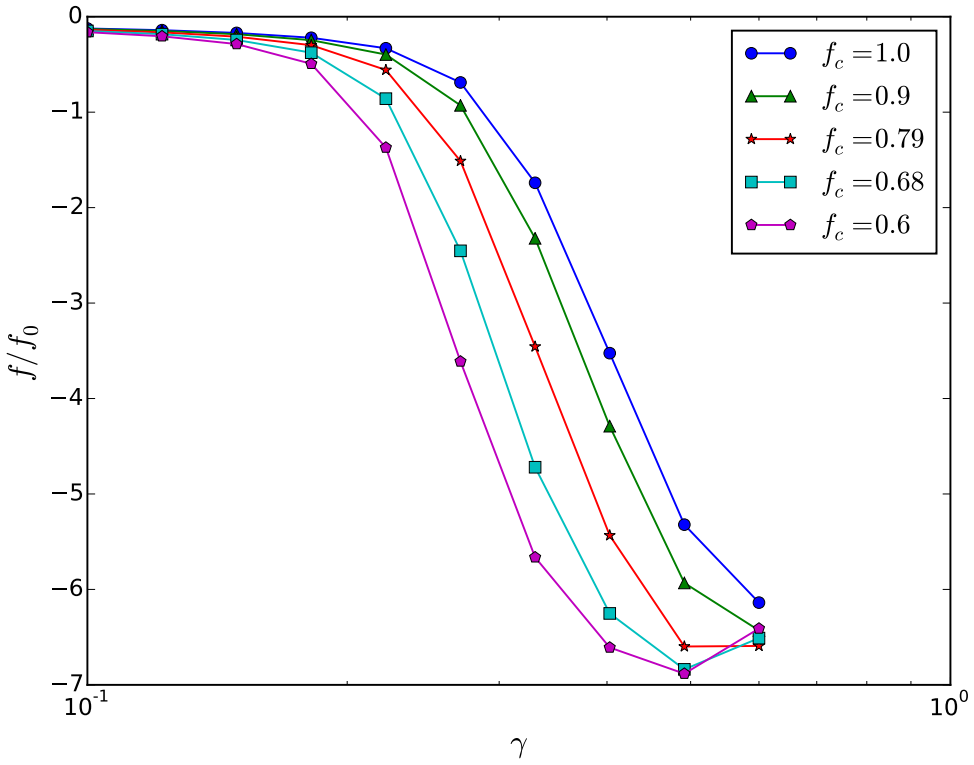

Figure 8.3: (Color Online) Distance to focal plane along the x_o axis from $z_o = 0$ plane of the outgoing beam as a function of the incoming beam's coherence and γ. Legend denotes the coherent fraction of the incoming beam. Horizontal axis is graduated on a logarithmic scale.

spatial incoherence.

CHAPTER 9

CONCLUSION

Our simulations show that dynamical diffraction of a Gaussian beam by an ideal crystal can produce fringes, increase the emittance by a factor 2, move the focal spot by mm's preserves the weak form of odd symmetry of Hermite-Gaussian modes. The fringes created by dynamical diffraction are rapidly smeared out by partial coherence, but might be useful as an experimental measure of coherence. The emittance and focal plane results have serious implications for beamlines that intend to deliver diffraction limited beams upon a sample.

Due to resource limits of our current code architecture, we could not explore the region $\gamma > 1$ in detail. Additionally, novel phenomena may be accessible in this regime. It might be possible to efficiently perform simulations for $\gamma > 1$ with a different code architecture.

APPENDIX A

ODD-EVEN SYMMETRY FOR HERMITE GAUSSIAN MODES

Exact values for I_{rx}^{mn} and I_{ry}^{mn} matrices are shown in tables A.1 and A.2. All numbers were represented by double precision floating point values in our code. This representation maintains 52 significant bits. A reduction in intensity by $\sim 10^{30}$ implies reduction in amplitude by $\sim 10^{15}$. This reduction in amplitude is equivalent to $\log_2 10^{15} \approx 50$ out of 52 bits worth of cancellation. It is reasonable to conclude that $I_{rx}^{mn} = 0$ ($I_{ry}^{mn} = 0$) whenever m (n) is odd

	n →				
m ↓	0	1	2	3	4
0	$10^{-0.0}$	$10^{-0.0}$	$10^{-0.0}$	$10^{-0.0}$	$10^{0.0}$
1	$10^{-31.1}$	$10^{-31.0}$	$10^{-31.1}$	$10^{-31.0}$	$10^{-31.0}$
2	$10^{-0.301}$	$10^{-0.301}$	$10^{-0.301}$	$10^{-0.301}$	$10^{-0.301}$
3	$10^{-31.1}$	$10^{-30.9}$	$10^{-30.9}$	$10^{-31.0}$	$10^{-31.1}$
4	$10^{-0.426}$	$10^{-0.426}$	$10^{-0.426}$	$10^{-0.426}$	$10^{-0.426}$

Table A.1: Amplitude-then-intensity integrated values (I_{rx}^{mn}, as defined in eq 6.5) in arb. units for $\gamma = 0.6$. Substantial ($\sim 10^{30}$) reductions in intensity for odd modes in x (indexed by m) suggests odd/even symmetry is pseudo-preserved after dynamical diffraction.

	n →				
m ↓	0	1	2	3	4
0	$10^{0.0}$	$10^{-31.9}$	$10^{-0.301}$	$10^{-31.8}$	$10^{-0.426}$
1	$10^{-0.111}$	$10^{-31.8}$	$10^{-0.412}$	$10^{-31.9}$	$10^{-0.537}$
2	$10^{-0.302}$	$10^{-32.1}$	$10^{-0.603}$	$10^{-32.1}$	$10^{-0.728}$
3	$10^{-0.383}$	$10^{-32.2}$	$10^{-0.684}$	$10^{-32.2}$	$10^{-0.809}$
4	$10^{-0.392}$	$10^{-32.2}$	$10^{-0.693}$	$10^{-32.2}$	$10^{-0.818}$

Table A.2: Amplitude-then-intensity integrated values (I_{ry}^{mn}, as defined in eq 6.5) in arb. units for $\gamma = 0.6$. Substantial ($\sim 10^{30}$) reductions in intensity for odd modes in y (indexed by n) suggests odd/even symmetry is pseudo-preserved after dynamical diffraction.

APPENDIX B

CODE EXECUTION GUIDE

The code developed as part of this thesis is managed using git version control software. This simplifies managing many versions of the code. Qgit is one of the many programs which can be used to visualize the development history of the code.

The development history of the code was logged in (PDF based) work-journals. To obtain any particular version of the code, first look at the accompanying work-journal. The captions for the plots in the work journal document how to obtain the code for generating that plot. A plot is a consistent point of documentation in both work-journal and git history.

There are three points of configuration for running the code. First, The plots in this thesis were generated using the framework5.py file, which in turn calls code in other files. This file controls how to vary the independent variable in any plot, computes dependent variables and writes the plots to disk. Second, the files in objasm folder control the relative configuration of incident beam, crystal and outgoing beams respectively. Third, the files in the objconf folder control the parameters of crystal and the beam.

BIBLIOGRAPHY

[1] James D Watson, Francis HC Crick, et al. Molecular structure of nucleic acids. *Nature*, 171(4356):737–738, 1953.

[2] D. Shechtman, I. Blech, D. Gratias, and J. W. Cahn. Metallic phase with long-range orientational order and no translational symmetry. *Phys. Rev. Lett.*, 53:1951–1953, Nov 1984.

[3] K. K. Kaneki, T. Nakamura, H. Ohkuma, J. Schimizu, Y. Shimosaki, K. Soutome, and M. Takao. Lattice Design of a Very Low-emittance Storage Ring for SPring-8-II. *Conf. Proc.*, C110904:942–944, 2011.

[4] Pedro F. Tavares, Simon C. Leemann, Magnus Sjöström, and ke Andersson. The MAXIV storage ring project. *Journal of Synchrotron Radiation*, 21(5):862–877, Sep 2014.

[5] Robert Hettel. DLSR design and plans: an international overview. *Journal of Synchrotron Radiation*, 21(5):843–855, Sep 2014.

[6] Oleg G. Shpyrko. X-ray photon correlation spectroscopy. *Journal of Synchrotron Radiation*, 21(5), Sep 2014.

[7] Pierre Thibault, Manuel Guizar-Sicairos, and Andreas Menzel. Coherent imaging at the diffraction limit. *Journal of Synchrotron Radiation*, 21(5):1011–1018, Sep 2014.

[8] Martin D. de Jonge, Christopher G. Ryan, and Chris J. Jacobsen. X-ray nanoprobes and diffraction-limited storage rings: opportunities and challenges of fluorescence tomography of biological specimens. *Journal of Synchrotron Radiation*, 21(5):1031–1047, Sep 2014.

[9] Christian G. Schroer and Gerald Falkenberg. Hard X-ray nanofocusing at low-emittance synchrotron radiation sources. *Journal of Synchrotron Radiation*, 21(5):996–1005, Sep 2014.

[10] Makina Yabashi, Kensuke Tono, Hidekazu Mimura, Satoshi Matsuyama, Kazuto Yamauchi, Takashi Tanaka, Hitoshi Tanaka, Kenji Tamasaku, Haruhiko Ohashi, Shunji Goto, and Tetsuya Ishikawa. Optics for coherent X-ray applications. *Journal of Synchrotron Radiation*, 21(5):976–985, Sep 2014.

[11] Boris W. Batterman and Henderson Cole. Dynamical diffraction of x rays by perfect crystals. *Rev. Mod. Phys.*, 36:681–717, Jul 1964.

[12] Melvin Lax, William H. Louisell, and William B. McKnight. From maxwell to paraxial wave optics. *Phys. Rev. A*, 11:1365–1370, Apr 1975.

[13] M. Meron, P. J. Viccaro, and B. Lin. Geometrical and wave optics of paraxial beams. *Phys. Rev. E*, 59:7152–7165, Jun 1999.

[14] A.E. Siegman. *Lasers*. University Science Books, 1986.

[15] C.G. Darwin M.A. Xxxiv. the theory of x-ray reflexion. *Philosophical Magazine Series 6*, 27(158):315–333, 1914.

[16] P. P. Ewald. Zur begrndung der kristalloptik. *Annalen der Physik*, 359(23):519–556, 1917.

[17] M. Laue. *Ergebnisse der Exakten Naturwissenschaften: Zehnter Band*, chapter Die dynamische Theorie der Röntgenstrahlinterferenzen in neuer Form, pages 133–158. Springer Berlin Heidelberg, Berlin, Heidelberg, 1931.

[18] S. van der Walt, S. C. Colbert, and G. Varoquaux. The numpy array: A structure for efficient numerical computation. *Computing in Science Engineering*, 13(2):22–30, March 2011.

[19] T. E. Oliphant. Python for scientific computing. *Computing in Science Engineering*, 9(3):10–20, May 2007.

[20] J. D. Hunter. Matplotlib: A 2d graphics environment. *Computing in Science Engineering*, 9(3):90–95, May 2007.

[21] David M. Beazley. Swig: An easy to use tool for integrating scripting languages with c and c++. In *Proceedings of the 4th Conference on USENIX Tcl/Tk Workshop, 1996 - Volume 4*, TCLTK'96, pages 15–15, Berkeley, CA, USA, 1996. USENIX Association.

[22] Ivan V. Bazarov. Synchrotron radiation representation in phase space. *Phys. Rev. ST Accel. Beams*, 15:050703, May 2012.

[23] M. Born, E. Wolf, and A.B. Bhatia. *Principles of Optics: Electromagnetic Theory of Propagation, Interference and Diffraction of Light*. Cambridge University Press, 1999.

[24] R. Shankar. *Principles of Quantum Mechanics*. Springer, 1994.

[25] Andrej Singer and Ivan A. Vartanyants. Coherence properties of focused X-ray beams at high-brilliance synchrotron sources. *Journal of Synchrotron Radiation*, 21(1):5–15, Jan 2014.

[26] Andrej Singer and Ivan A. Vartanyants. Modelling of partially coherent radiation based on the coherent mode decomposition. *Proc. SPIE*, 8141:814106–814106–9, 2011.

[27] I A Vartanyants and A Singer. Coherence properties of hard x-ray synchrotron sources and x-ray free-electron lasers. *New Journal of Physics*, 12(3):035004, 2010.

[28] A. Starikov and E. Wolf. Coherent-mode representation of gaussian schell-model sources and of their radiation fields. *J. Opt. Soc. Am.*, 72(7):923–928, Jul 1982.

[29] Kwang-Je Kim. Brightness, coherence and propagation characteristics of synchrotron radiation. *Nuclear Instruments and Methods in Physics Research Section A: Accelerators, Spectrometers, Detectors and Associated Equipment*, 246(13):71 – 76, 1986.

[30] Martin J Bastiaans et al. Application of the wigner distribution function in optics, 1997.